1   **Ion Adsorption at Clay Mineral Surfaces: The Hofmeister Series for Hydrated Smectite**

2   **Minerals**

3   Thomas Underwood, Valentina Erastova, H. Chris Greenwell

4   Durham University

5

6   Department of Earth Sciences,

7   Durham University,

8   Science Labs,

9   Durham DH1 3LE

10 **ABSTRACT**

11   Many important properties of clay minerals are defined by the species of charge-

12 balancing cation. Phenomena such as clay swelling and cation exchange depend upon the cation

13 species present and it is therefore important to understand how the cations bind with the mineral

14 surface at a fundamental level. In the present study, the binding affinities of several different

15 charge-balancing cations with the basal surface of the smectite clay montmorillonite have been

16 calculated using molecular dynamics in conjunction with the well-tempered metadynamics

17 algorithm. The results follow a Hofmeister series of preferred ion adsorption to the smectite

18 basal surfaces of the form:

$$K^+ > Na^+ > Ca^{2+} > Cs^+ > Ba^{2+}$$
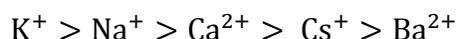
19 The results also reveal the energetically favorable position of the ions above the clay basal

20 surfaces. Key features of the free energy profiles are illustrated by Boltzmann population

21 inversions and analyses of the water structures surrounding the ion and clay surface. The results

22 show that weakly hydrated cations (K^+ and Cs^+) preferentially form inner-sphere surface

23 complexes (ISSC) above the ditrigonal siloxane cavities of the clay, whilst the more strongly

24 hydrated cations (Na^+) are able to form ISSCs above the basal oxygen atoms of the clay surface.

25 The strongly hydrated cations (Na^+, Ca^{2+} and Ba^{2+}) preferentially form outer-sphere surface

26 complexes. The results provide insight into the adsorption mechanisms of several ionic species

27 upon smectite clay minerals, and are relevant to many phenomena thought to be affected by

28 cation-exchange, such as nuclear waste disposal, herbicide/pesticide-soil interactions and

29 enhanced oil recovery.

30

33   **INTRODUCTION**

34   Clays are naturally occurring layered phyllosilicate minerals which are known to play an

35   important role in many geochemical processes, whether within marine systems, terrestrial soils

36   or within the subsurface in aquifers and oil reservoirs (Bergaya *et al.,* 2006). Owing to their high

37   surface area, permanent negative charge and cation exchange properties, smectite clay minerals

38   have found an increasing multitude of practical applications and have been extensively studied

39   using analytical laboratory based techniques. In recent years, computational techniques, such as

40   molecular dynamics (MD) and *ab-initio* calculations (including density functional theory –

41   DFT), have become increasingly beneficial in helping improve our understanding of clay mineral

42   properties at the atomistic level ((Greenwell, 2006), (Suter J. L., 2009)).

43   Three types of clay mineral surfaces are apparent: (i) the external basal surfaces, (ii) the

44   external clay edges; (iii) the interlayer basal surfaces. The adsorption and exchange of cations at

45   the different clay minerals surfaces can comprehensively alter the physical and chemical

46   properties of the clay mineral. Interlayer bound potassium, for example, acts as a swelling

47   inhibitor, preventing hydration and expansion of the interlayer region, whilst sodium promotes

48   swelling when present in smectite-like clay minerals (Boek *et al.,* 1995). Furthermore, owing to

49   their use as a barrier material in underground nuclear waste repositories it is becoming

50   increasingly important to understand how radioactive cations, such as barium and cesium, adsorb

51   to clay mineral surfaces, with potentially significant ramifications for nuclear waste repository

52   design and operation (Ngouana *et al.,* 2014). Since the behavior of clay minerals depend upon

53   the species of charge-balancing cation, it is important to understand how the cation binds with

54   the mineral surface, and how the cation's affinity to the surface differs from ion to ion; however,

55   studying the behaviour of cations at clay mineral surfaces and within interlayers is particularly

56   challenging. Nuclear magnetic resonance (NMR) studies have been undertaken on non-

57   paramagnetic synthetic clays offering insight on ion dynamics and distribution (Bowers *et al.,*

58   2008), while the use of quasi-elastic neutron scattering (QENS) on well-ordered vermiculite clay

59   gels, as well as smectites, has allowed the study of cation/water structure in interlayers

60   ((Swenson *et al.,* 2000), (Marry *et al.,* 2013)). Additional insight into swelling energetics and

61   structure has been obtained from computer simulation of hydrated clay minerals ((Boek *et al.,*

62   1995), (Shroll and Smith*,* 1999), (Boek and Sprik.*,* 2003)).

63   A key property of many clay minerals is cation-exchange, where a more labile cation is

64   substituted by a less labile one to modify the clay mineral activity. The traditional view of

65   alkaline metal ion selectivity for cation-exchange follows a Hofmeister-like series (Hanshaw,

66   1964):

$$K^+ \approx Cs^+ > Na^+ > Ba^{2+} \approx Ca^{2+}$$
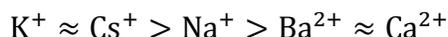
67   The reasoning for this sequence have been postulated through (at least) two arguments:

68   1) The ratio of hydrated cation size to interlayer spacing ((Gast, 1969), (Gast, 1972)),

69   whether the hydrated ion can fit within the steric cavities of the interlayer spacing;

70   2) The cations' ability to partially dehydrate at the mineral surface and thus form strong

71   inner-sphere surface complexes (Eisenman, 1962).

72

73   Whilst many historical studies of the Hofmeister series have examined the hydration

74   properties of the ions, in recent years it has become increasingly apparent that ion-

75   macromolecule interactions also play a dominant role (Zhang and Cremer, 2006).

76   Previous computational work has been able to elucidate some of the properties of cation-

77   exchange clay systems. It has previously been shown that whilst the binding energy between

78   potassium and montmorillonite is greater than that between cesium and montmorillonite, the

79   cesium-montmorillonite system is overall more stable due to the decreased enthalpy of hydration

80   of the potassium over the cesium in the solvent phase (Teppen and Miller, 2006). The result

81   shows it is important to consider not only the effect of the ion interacting with the mineral

82   surface, but also with the bulk solvent phase. Previously, this has been achieved using an explicit

83   solvent bath (Rotenberg *et al.,* 2007) or through the use of thermodynamic cycles (Rotenberg *et*

84   *al.,* 2009).

85   In this present study, classical molecular dynamic simulations have been used in

86   conjunction with well-tempered metadynamics to determine the free energy of adsorption of, as

87   well as the competition between, cations at the hydrated basal surfaces of the smectite clay

88   mineral montmorillonite. The following simulations are particularly pertinent for understanding

89   of the phenomenon of multicomponent cation-exchange during low salinity enhanced oil

90   recover, whereby organic matter, bridged to the surface through divalent cations, becomes

91   desorbed from the basal surface of a clay mineral (Underwood *et al.,* 2015).

92   **METHODS**

93   *Model Setup*

94   The clay unit cell used in this study was a Wyoming-like montmorillonite with atomic

95   coordinates taken from the *American Mineralogist Crystal Structure Database* ((Downs and

96   Hall-Wallace, 2003), (Viani *et al.,* 2002)) and with stoichiometry:

$$M^+ [Al_3Mg_1][Si_8O_{20}](OH)_4 . nH_2O$$

97   In this model the octahedral sheets of the clay contained one Mg atom for every three Al atoms,

98   whilst both tetrahedral sheets contained no isomorphic substitutions. The resulting unit cell

99   possessed a single net negative charge, corresponding to a surface charge density of

100   approximately 0.35 *C m⁻²*. Periodically replicated super-cells were generated containing one

101   layer of montmorillonite, composed of 18 unit cells (6 x 3 x 1), with dimensions of

102   approximately 30 x 30 x 100 Å, and a pore-spacing of approximately 90 Å (Figure 1).

103   Montmorillonite structures initially occupied the region $0 < z < 7$ Å in all the following

104   simulations, and the clay position varied little over all timescales modelled. The simulation

105   super-cells were subsequently hydrated (with approximately 2500 water molecules) and the

106   requisite number of cations added to the system to charge balance the montmorillonite surface.

107   In total, five independent systems were set up differing according to the type of charge-balancing

108   cation. The cations considered in this study were: sodium (Na^+), potassium (K^+), cesium (Cs^+),

109   calcium (Ca^{2+}) and barium (Ba^{2+}).

110   The clay mineral has been modelled using the ClayFF force field (Cygan *et al.,* 2004),

111   which is specifically parameterized to model layered minerals. The ClayFF force field is

112   designed such that the entire interactions within, and structure of, the clay is described wholly by

113   the non-bonded Lennard-Jones and Coulomb potentials (hydroxyl groups are bonded as an

114   exception). The standard SPC water model (Berendsen *et al.,* 1987) has been used to

115   parameterize the solvent. Ion parameters are taken from a variety of sources and are consistent

116   with the ClayFF and SPC force fields ((Smith and Dang (I), 1994), (Smith and Dang (II), 1994)

117   (Koneshan *et al.,* 1998),(Aaqvist, 1990)), (Cygan *et al.,* 2004).

118

119   ***Equilibration Details***

120   All simulations have been initialized with an energy minimization run to reduce any

121   excessive force on any one atom. This was accomplished using a steepest descents algorithm,

122   with convergence achieved once the maximum force on any one atom was less than 10 *kJ mol^{-1}*

123   Å^{-1}. Subsequently, equilibration simulations were run for a 10 *ns* period in the constant number

124   of particles, pressure and temperature (NPT) ensemble at 300 *K* and 1 *bar* using a velocity-

125   rescale Berendsen thermostat, temperature coupling constant set to 0.1 *ps*, and a semi-isotropic

126   Berendsen barostat, with pressure-coupling constant 1 *ps*. The Berensden thermostat and barostat

127   offered swift equilibration of the system, and convergence was adjudged to have been attained

128   once both the *z*-spacing and potential energy had converged.

129

130   ***Metadynamic Details***

131   Subsequent to equilibration, the super-cell was translated along the *z*-axis such that the

132   apical oxygen atoms of the silicate sheet of the lowest clay basal surface lay upon the *z* = 0 Å

133   plane. Before any free energy calculations were carried out, the clay model was fixed in place as

134   a rigid structure. Subsequently, a single cation was chosen at random to be the test ion, upon

135   which the free energy calculations have been performed. All other ions in the system were free to

136   move according to the force fields used in the simulations.

137   The well-tempered metadynamics algorithm was used to explore the free energy curve of

138 the clay-ion-water system as a function of the clay-ion separation (i.e. the reaction coordinate).

139 During the metadynamics simulation the forces calculated with conventional molecular

140 dynamics are modulated by adding Gaussian functions to the Hamiltonian at points along the

141 reaction coordinate (Barducci *et al.,* 2008). Here, twenty-five separate well-tempered

142 metadynamic simulations were run, five for each cation type. It is important to run multiple

143 ensemble simulations when calculating equilibrium thermodynamic properties, such as binding

144 energies, since any one simulation is unlikely to sufficiently sample all of the phase-space

145 required to satisfy the ergodic hypothesis (Coveney and Wan, 2016). Five separate ensemble

146 simulations were deemed sufficient to reduce the total uncertainty in the free energy profiles

147 generated using the metadynamic algorithm in this work. Each metadynamic simulation was run

148 for a duration of 200 *ns* at 300 *K* in the constant number of particles, volume and temperature

149 (NVT) ensemble. Gaussian functions with an initial height of 1.20 *kJ/mol*, a width of 0.10 Å, and

150 a bias factor of 10 were applied to the Hamiltonian every 0.5 *ps*. Convergence of the well-

151 tempered metadynamics algorithm was ensured by observing that the Gaussian height tended to

152 zero throughout all well-tempered metadynamic simulations. Checks were also made to ensure

153 that the test ion sampled all of the available planar *xy*-space, in conjunction with clay-ion

154 separation space.

155   Due to the translational symmetry of the clay mineral, additional bias potentials were

156 added to the test ion. This constrained the ion within a single unit cell of the montmorillonite

157 surface. Any additional sampling would simply increase computational time, yet yield no

158 additional information. This constraint was achieved using a spring-like bias of the form:

159     $$V_{wall}(x) = k(x - x_{max})^4 \in x > x_{max} \qquad\qquad (1)$$

160   where k is the elastic spring constant of the wall, set to 500 kJ/mol, and x_{max} is the lower limit of

161   the wall. Similar boundaries were setup to constrain the lower bounds of the test ion in the x-

162   direction, to constrain the ion in the y-direction, as well as to keep the test ion within 10 Å of the

163   mineral surface.

164

165   *Simulation Details*

166   All MD simulations were performed using GROMACS version 4.6.7 (Pronk, et al., 2013)

167   with the Particle-Mesh-Ewald summation method for determining the electrostatic contribution,

168   with a real-space electrostatic cut-off of 12 Å, a reciprocal space precision of 10^{-5}, in addition to

169   a van der Waals cut-off distance of 1.2 Å. The well-tempered metadynamic algorithm has been

170   implemented using PLUMED 2.1.2 (Bonomi *et al.,* 2009) (Tribello *et al.,* 2014), which works in

171   conjunction with GROMACS, whilst all images of the simulated structures have been produced

172   using VMD 1.9.2 (Humphrey, 1996).

173

174   *Analysis Details*

175   All free energy analyses have been carried out using the internal tools for GROMACS

176   4.6.7 and PLUMED 2.1.2 (Bonomi *et al.,* 2009) (Tribello *et al.,* 2014). The Python module

177   MDAnalysis 0.13 (Michaud-Agrawal *et al.,* 2011) and Matplotlib 1.5.1 (Hunter, 2007) were used

178   to further analyze simulation trajectories and generate figures of water densities and radial

179   distribution functions (RDFs). The plotted free energy profiles present the average free energy at

180   each point along the reaction coordinate as a bold line and the relative error (plus-minus) is

181   presented in the shaded area. The values of individual binding energies are given with the

182   corresponding standard error as plus-minus. All ion density profiles (dotted lines in the free

183   energy profiles) have been calculated using the last 5 *ns* of the 10 *ns* equilibration period, i.e.

184   from an unbiased simulation.

185   **RESULTS**

186   It is initially worth highlighting the general shape of the free energy curves (Figure 2).

187   After a short range repulsion between ion and mineral surface, and beyond (often several)

188   minima, the free energy profiles plateau. In the long clay-ion separation limit, this plateau can be

189   decomposed as a combination of clay (F_{self}^{clay}), ion (F_{self}^{ion}) and solvent (F_{self}^{water}) self-energies; clay-

190   water ($F_{hydration}^{clay}$) and ion-water ($F_{hydration}^{ion}$) hydration energies; as well as long-range

191   interaction terms ($F_{electostatic}^{clay-ion}$). Namely the binding free energy (F), can be expressed as:

192          $$\lim_{z \to \infty} F(z) = F_{self}^{clay} + F_{self}^{ion} + F_{self}^{water} + F_{hydration}^{clay} + F_{hydration}^{ion} + F_{electostatic}^{clay-ion}(z) \quad (2)$$

193   This means that the overall binding energy ($\Delta F_{Binding}$) of the ion to the surface can be calculated

194   as:

195          $$\Delta F_{Binding} = F(z_{min}) - \lim_{z \to \infty} F(z) \qquad (3)$$ where z_{min} is the location of the global energy

196   minimum with respect to clay-ion separation.

197   Note that at sufficiently large z, the individual self-energies of the unbound system and hydration

198   terms in equation 2 are independent of z, since the hydration shells of the ion and clay no longer

199   overlap. Thus, at large z, when comparing binding energies between different ion species, one

200   needs only to consider the difference between the long-range clay-ion electrostatic term. Since

201   all simulations have been run at the same temperature (300 K) and ionic strengths the long-range

202   electrostatic term, which can be described through Poisson-Boltzmann theory, is postulated to be

203   equal for all different ions at any arbitrary z. It is therefore justified to normalize the free energy

204   profiles subject to the boundary condition that for large clay-ion separation:

205    $\lim_{z \to \infty} F(z) = 0$ (4)Following this argument, a direct comparison of

206   the binding free energies differences between dissimilar species of monovalent and divalent

207   cations have been calculated (Table 1).

208

209   ***Free Energy Profiles:***

210   The free energy profile for all the systems considered (Figure 2), highlight several points

211   of interest along the reaction-coordinate. These are highlighted by the points (A), (B), (C), (D)

212   and (E) across the top of the figure. To be consistent, the points correspond to the coordination

213   states of the ion. In brief, (A) corresponds to a primary inner-sphere surface complex (ISSC); (B)

214   corresponds to a secondary ISSC; (C) corresponds to outer-sphere surface complex (OSSC) and

215   (D) corresponds to a secondary hydration shell surface complex (SHSSC). These terms shall be

216   explained in the following sections. The point (E) corresponds to a clay-ion separation of 10 Å,

217   the maximal distance of the reaction-coordinate in the metadynamic simulations.

218

219   ***Na-Montmorillonite:***

220   The free energy profile for the sodium-montmorillonite system (Figure 2 - Na) shows that

221   at close separation distances (less than 2 Å) the montmorillonite-ion interaction is entirely

222   repulsive. This represents the close-range repulsion between clay and ion due to electron wave-

223   function overlap. Beyond this, the ion experiences three individual clay-ion separations of

224   (meta)stable equilibria. The global minimum, and thus the most energetically favorable

225   montmorillonite-sodium separation is at 3.8 Å, with a binding energy of -9.00±0.35 *kJ/mol*

226   (Figure 2 – Na(C)). A secondary, metastable minimum, is located nearer to the clay surface, at a

227   clay-sodium distance of 2.3 Å, with a binding energy of -2.76±0.43 *kJ/mol* (Figure 2 - Na(B)). A

228   third, metastable minimum, is located further from the clay surface, at a separation value of 6 Å

229   and with a binding energy of -3.68±0.37 *kJ/mol* (Figure 2 - Na(D)).

230   The global minimum corresponds to a system where the sodium cation is fully hydrated,

231   and the ion's solvation shell is associated to the mineral surface *via* hydrogen bonding. This can

232   be observed in the overlapping water structures of the first hydration shell of the ion with the

233   first hydration layer of the clay (Figure 3 - Na(C)). This phenomenon is well known, and referred

234   to as an outer-sphere solvation complex (OSSC). In contrast, the metastable minimum nearer the

235   clay surface corresponds to an inner-sphere solvation complex (ISSC), whereby the cation is

236   only partially hydrated, and is directly adsorbed to the mineral surface *via* electrostatic

237   interactions (Figure 3 - Na(B)). The metastable minimum farthest away from the clay surface

238   corresponds to where the second hydration shell of the sodium ion overlaps with the first

239   hydration layer of the clay (Figure 3 - Na(D)). This situation is observed for several cations and

240   shall be hereafter denoted as a secondary hydration shell surface complex (SHSSC). Also

241   presented is the water structure surrounding the ion and clay at a clay-ion separation of 10 Å

242   (Figure 3 - Na(E)). It can be noted that at such distance, the hydration layers of the clay and ion

243   no longer overlap.

244   The radial distribution functions (RDFs) between sodium ion and water/basal clay

245   oxygen further reiterate that the minima correspond to ISSC and OSSC. It can be seen that for

246   the ISSC (Figure 4 - Na(B)), the basal clay oxygen atoms are shared with water oxygen atoms in

247   the first coordination shell of the ion. In contrast, for the OSSC (Figure 4 - Na(C)), the basal clay

248   oxygen atoms are contained within the second coordination shell of the ion. For the SHSSC

249   (Figure 4 - Na(D)), the clay basal oxygen atoms contribute to the third coordination shell of the

250   sodium ion. Also presented is the RDF for the system at a clay-ion separation of 10 Å (Figure 4 -

251   Na(E)). In this case the hydration layers of the ion and clay no longer interact and the resulting

252   RDF is that of the sodium ion with bulk water.

253   The planar density of the ion above the mineral surface shows that, for the ISSC, the

254   sodium ion is extremely localized above a single basal clay oxygen (Figure 5 - Na(B)). In

255   contrast, the OSSC is less localized above the clay basal surface (Figure 5 - Na(C)), with a

256   preference to be located above one of the hexagonal siloxane cavities of the mineral surface. For

257   the SHSSC and beyond, the ion's position above the basal clay surface is no longer localized,

258   and is homogeneously dispersed across the unit cell (Figure 5 - Na(C) and Na(D)).

259

260   ***K-Montmorillonite:***

261   The free energy profile for potassium (Figure 2 - K) presents several features similar to

262   that of sodium. Again, it can be seen that beyond the typical close distance repulsion, three

263   separate (meta)stable minima are observed. The global minimum, in this instance, is located near

264   the surface of the mineral, at a montmorillonite-potassium separation of 1.3 Å, with a binding

265   energy of -10.56±1.29 *kJ/mol* (Figure 2 - K(A)). The next most stable minimum is located at 4.7

266   Å, with a binding energy of -3.83±0.37 *kJ/mol* (Figure 2 - K(C)). There is also a metastable

267   minimum between these two points at a clay-potassium separation of 2.6 Å with a binding

268   energy of -2.46±0.70 *kJ/mol* (Figure 2 - Na(B)).

269   Focusing on the global energy minimum (point A), both the water structure (Figure 3 -

270   K(A)) and the RDF (Figure 4 - K(A)) reveal that the ion forms an ISSC in its most energetically

271   favorable state. In particular, the RDF shows that the first coordination shell of the potassium ion

272   is largely composed of clay oxygen atoms. The *xy*-planar density of the potassium ion in its ISSC

273   state (Figure 5 - K(A)) shows that the ion is extremely localized above the hexagonal cavities of

274   the clay surface. This behavior is in contrast to the ISSC observed for sodium. The terms primary

275   ISSC and secondary ISSC are here introduced to denote the difference between these two

276   different forms of ISSC. A primary ISSC denotes an ion that sits above one of the hexagonal

277   cavities of the clay surface, whilst the term secondary ISSC denotes that the ion sits above one of

278   the basal oxygen atoms of the clay.

279   The least energetically favorable metastable minimum is located at point (B) in the free

280   energy profile (Figure 2 – K(B)). The water structure (Figure 3 - K(B)) and RDF (Figure 4 –

281   K(B)) indicate that this minimum is also an ISSC. The *xy*-planar density of the ion above the

282   surface (Figure 4 - K(B)) indicates that this is a secondary ISSC. The results show that potassium

283   can stably form both primary, and secondary, inner-sphere surface complexes.

284   The most energetically favorable metastable minimum is located at point (C) in the free

285   energy profile (Figure 2 – K(C)). Here the potassium ion forms an OSSC, as the first hydration

286   shell of the ion overlaps with the first hydration layer of the clay (Figure 3 - K(C)). The RDF

287   (Figure 4 - K(C)) also highlights that the basal clay oxygen atoms coordinate within the second

288   hydration shell of the potassium cation. Like the sodium ion, the OSSC of potassium is loosely

289   localized above the hexagonal siloxane cavities of the basal surface, as evidenced by the *xy*-

290   planar density distribution (Figure 5 - K(C)). Beyond this point, the potassium ion is not

291   observed to form a SHSSC and moves freely across the *xy*-plane (Figure 5 - K(E)).

292

293   ***Cs-Montmorillonite:***

294   The free energy diagram for the cesium-montmorillonite system (Figure 2 - Cs) is very

295   similar to that of potassium. Again, three separate minima are observed. The global energy

296   minimum is at a montmorillonite-cesium separation of 2.0 Å with a binding energy of -

297   8.34±0.40 *kJ/mol* (Figure 2 - Cs(A)). The secondary minimum is at a clay-ion distance of 2.7 Å

298   with a binding energy of -7.51±0.38 *kJ/mol* (Figure 2 - Cs(B)) and the tertiary minimum is

299   located at a clay-ion distance of 4.6 Å with a binding energy of -4.64±0.26 *kJ/mol* (Figure 2 -

300   Cs(C)).

301   The global minimum of cesium forms an ISSC as can be observed through the water

302   structure (Figure 3 - Cs(A)) and cesium-oxygen RDF results (Figure 4 - Cs(A)). Like potassium,

303   the global energy minimum of cesium is localized above the hexagonal siloxane cavities of the

304   clay surface (Figure 5 - Cs(A)) and is therefore observed to form primary ISSCs.

305   The second and third minima of cesium correspond to a secondary ISSC and OSSC

306   respectively. This is evidenced by the overlapping of the water structures surrounding the ion

307   and clay (Figure 3 - Cs (B) and Cs(C)), the overlapping oxygen atoms in the RDFs (Figure 4 -

308   Cs(B) and Cs(C)), as well as the ion localizations above the *xy*-plane (Figure 5 - Cs(B) and

309   Cs(C)). Much like potassium therefore, cesium readily forms both secondary ISSCs and OSSCs.

310   Unlike potassium however, the secondary ISSC is more energetically stable than the OSSC.

311

312   ***Ca-Montmorillonite:***

313   In contrast with the results for other ions presented so far, the free energy profile for

314   calcium shows only one stable minimum (Figure 2 – Ca). This minimum is at a clay-ion distance

315   of 3.8 Å and has a binding energy of -16.76±0.41 *kJ/mol* (Figure 2 - Ca(C)). The water structures

316   surrounding the calcium and clay in conjunction with the RDFs between ion and oxygen atoms

317   show that this global energy minimum is an OSSC. The water structure (Figure 3 – Ca(C))

318   shows that the first hydration shell of the calcium overlaps with the first hydration layer of the

319   clay basal surface. Furthermore, the RDF (Figure 4 - Ca(C)) indicates that the basal oxygen

320   atoms of the clay contribute to the second hydration shell of the calcium. The planar density of

321   the calcium ion in its global OSSC state (Figure 5 - Ca(C)) presents that the calcium ion sits

322   above the hexagonal siloxane cavities of the basal surface of the clay, in agreement with the

323   trends observed for the monovalent ions. Nonetheless, the OSSC for the calcium ion is more

324   localized compared to the OSSCs for monovalent ions.

325   Point (D) in the calcium system refers to the sudden change in gradient of the free energy

326   curve. This change in gradient is due to the completion of the second hydration shell of the

327   calcium ion as is shown in the water density profile (Figure 3 - Ca(D)). At this point the clay no

328   longer contributes to the hydration shells of the calcium ion, as is confirmed by comparing the

329   RDF between calcium and basal clay oxygen atoms with the RDF between calcium and all

330   oxygen atoms (Figure 4 - Ca(D)). The planar density profile for point (D) (Figure 4 - Ca(D))

331   shows that calcium ion sits above the either the basal oxygen of silicon atoms of the clay.

332   Therefore, the aforementioned completion of the second coordination shell of the calcium ion is

333   achieved with water oxygen atoms.

334

335   ***Ba-Montmorillonite:***

336   The free energy profile of the montmorillonite-barium system (Figure 2 - Ba) presents

337   several interesting features not observed in the free energy profile for calcium. The global energy

338   minimum (point C) corresponds to a clay-ion separation of 4.2 Å with a binding energy of -

339   16.66±1.46 *kJ/mol* (Figure 2 - Ba(C)). There is also a second, energetically expensive,

340   metastable minima in the free energy curve (point A). This metastable minimum is located at a

341   clay-ion separation value of 1.9 Å and has a binding energy of +18.26±3.55 *kJ/mol* (Figure 12 -

342   Ba(A)), i.e. energy is required to place the ion into this metastable minimum. Two plateaus can

343   also be seen in the free energy profile of barium. Point (B) is at a clay-ion separation of 2.6 Å

344   and has a binding energy of -0.54±1.82 *kJ/mol* (Figure 2 - Ba(B)), whilst point (D) is at a clay-

345   ion separation of 5.8 Å and has a binding energy of -8.38±1.25 *kJ/mol* (Figure 2 - Ba(D)).

346   The water density profiles and RDFs of the barium-montmorillonite system explain how

347   the ion binds with the mineral surface. At points (A) and (B), the ion is directly coordinated by

348   basal oxygen atoms, forming primary and secondary ISSCs respectively (Figures 3 and 4 –

349   Ba(A) and Ba(B)). The water structure shows that the global energy minimum occurs when the

350   barium ion is an OSSC (Figure 3 - Ba (C). In such an occurrence, the basal oxygen atoms of the

351   clay contribute to the second hydration shell of the cation, as can be seen in the corresponding

352   RDF (Figure 4 - Ba(C)). The plateau at point (D) of the free energy curve occurs when the

353   second hydration layer of the barium ion begins to completely coordinate with water oxygen

354   atoms (Figure 3 - Ba(D)).

355   Analysis of the planar density of barium above the *xy*-plane of the clay shows that the

356   two ISSCs are extremely localized above a cavity of the clay siloxane (Figure 5 - Ba (A)) or

357   directly above basal oxygen atoms (Figure 5 - Ba (B)) for the metastable minimum (point A) and

358   plateau (point B) respectively. Similar to all other OSSCs, the OSSC of barium is localized

359   above one of the hexagonal siloxane cavities of the clay (Figure 5 - Ba (C)), whilst at all clay-ion

360   separations greater than this distance, the cation freely traverses across the *xy*-plane of the clay

361   mineral (Figure 5 - Ba (D)).

362

363   **DISCUSSION**

364   The results show that the charge-balancing cations of montmorillonite can form four

365   different stable surface complexes: a primary ISSC located above the siloxane cavity of the basal

366   clay surface; a secondary ISSC located above a basal oxygen atom; an OSSC loosely located

367   above siloxane cavity; and a SHSSC, which is due to the overlap of the ion's second hydration

368   sphere with the clay minerals first hydration layer. No further surface complexes were observed

369   in the simulations.

370   The formation of two separate ISSCs has been noted in the literature previously. In

371   particular, it has been shown that weakly hydrated interlayer cations (K^+, Cs^+) form ISSCs above

372   the siloxane cavity of the clay interlayer ((Park and Sposito, 2002), (Nakano *et al*., 2003), (Marry

373   and Turq, 2003)) whilst strongly hydrated cations (Na^+) form ISSCs on tetrahedral charge sites

374   ((Boek *et al.,* 1995), (Chang *et al*., 1995), (Marry and Turq, 2003)). The results presented here

375   supplement this previous work, and further suggest that the formation of ISSCs for strongly

376   hydrating cation can occur in the absence of tetrahedral charge substitutions. Moreover, they

377   implicate that the formation of different surface complexes is related to the hydration properties

378   of the cation. The stable surface complexation of a cation is related to the hydrated radii of the

379   atom, which is, in turn, inversely proportional to the charge/size ratio of the ion (Table 2).

380   The weakly hydrated cations, K^+ and Cs^+, have very similar hydration radii (Table 2), and

381   therefore exhibit similar behavior. In both cases, the primary ISSC is the most energetically

382   favorable state of the ion, and the secondary ISSC and OSSC are metastable. The strongly

383   hydrated monovalent cation, Na^+, forms secondary ISSCs, OSSCs and SHSSCs, and is

384   energetically most stable in its OSSC. Similarly, divalent cations form globally stable OSSCs, in

385   concordance with the relevant literature ((Brown and Kevan, 1988), (Papelis and Hayes, 1996),

386   (Chen and Hayes, 1999), (Strawn and Sparks, 1999), (Greathouse *et al*., 2000)). Barium exhibits

387   interesting behaviour; it is an ion that can form stable primary ISSCs and OSSCs, with plateaus

388   in the free energy profile associated with the formation of a secondary ISSC and a SHSSC

389   (Zhang *et al.*, 2001). This is due to the larger atomic radius of barium compared to calcium,

390   whereby the charge/size ratio of barium lies somewhere between that of calcium and sodium.

391   Overall, the results are well converged. The largest errors encountered are for the free

392   energy profiles of potassium and barium. Since the free energy profile for barium contains

393   several plateaus and minima, the metadynamic algorithm requires more simulation time to

394   sample all clay-ion separation phase space compared to other ions. The potassium ion contains a

395   large error due to the lack of convergence in the global energy minimum. This is due to the

396   complex coordination of oxygen atoms to the potassium ion, and shall be elaborated upon further

397   in the following sections.

398

399   *Accuracy of Results:*

400   To further analyze the accuracy of the free energy profiles, a comparison is made

401   between the equilibrium density profile of the unbiased equilibration simulation with the density

402   profile derived from the free energy. The cation density surrounding the montmorillonite surface

403   is derived from the free energy profile as:

404    $$n(d) \propto \exp\left(\frac{-\Delta G(d)}{k_B T}\right)$$ (5) where n(d) is the density profile of the ion

405   surrounding the clay, $\Delta G(d)$ is the corresponding free energy at the point d and $k_B T$ is the

406   thermal energy at temperature T. Strictly speaking, since the simulations have been carried out in

407   the NVT ensemble, the calculated free energy is the Helmholtz free energy. However, because

408   the simulations had been previously equilibrated in the NPT ensemble, one can assume that the

409   Helmholtz and Gibbs free energies are equivalent, under the assumption that the metadynamic

410   bias applied to the ion does not alter the average z-spacing of the simulation box.

411   The analysis shows that the free energy profiles capture the overall trends observed in the

412   unbiased density profile (Figure 6). In particular, the strongly hydrating cations (Na^+, Ca^{2+} and

413   Ba^{2+}) density profiles match extremely well. The free energy profiles generated for Na^+, Ca^{2+}

414   and Ba^{2+} capture the essential details of the equilibrium density profile and agrees with previous

415   results of cationic distribution surrounding montmorillonite basal surfaces (Rotenberg *et al.,*

416   2010) (Greathouse *et al.,* 2015). The ion densities calculated from the free energy profiles for the

417   weakly hydrating cations (K^+ and Cs^+) vary considerably compared to the equilibrium density. In

418   the case of potassium, the metadynamic density underestimates the the proportion of secondary

419   ISSCs and OSSCs, suggesting that the free energy calculation overestimates the global binding

420   energy of potassium to montmorillonite. In contrast, the metadynamic density overestimates the

421   proportion of secondary ISSCs and OSSCs for cesium. This suggests that the free energy profile

422   underestimates the global binding energy of cesium. Clearly, there is a phenomenon occurring

423   for the weakly hydrated cations, causing their binding energies to be less accurate compared to

424   their more strongly hydrated counterparts.

425

426   **Coordination Analysis**

427   The lower accuracy in the binding energies for potassium and cesium can be explained by

428   examining the coordination number of the ion in its most energetically stable state. This is

429   calculated by integrating under the first peak of the radial distribution function (RDF) for each

430   ion (Table 3). Note that in bulk, the coordination of ions ranges between 6 to 8 oxygen atoms,

431   systematically 1 to 2 counts over the expected literature values (Varma, 2006). In the SHSSC

432   and OSSC states, the ion remains completely coordinated with water oxygen atoms. In the

433   secondary ISSC the strongly hydrated sodium ion is coordinated by five water oxygen atoms and

434   one clay oxygen atom. This, along with the *xy*-planar density for sodium in its ISSC, proves that

435   the strongly hydrated monovalent cation coordinates directly above a single basal clay oxygen

436   atom. The coordination of the secondary ISSCs for the weakly hydrating cations, potassium and

437   cesium, show that 2 to 3 clay oxygen atoms are contained within the ions first coordination shell.

438   The secondary ISSCs for potassium and cesium complex with a triad of basal oxygen atoms, in

439   keeping with previous literature (Park and Sposito, 2002).

440   Profoundly, for the primary ISSC of potassium and cesium, the ion is coordinated with

441   six oxygen clay atoms, as well as four/six water oxygen atoms. This drastic change in the total

442   coordination number of potassium and cesium is the reason that the binding energy calculations

443   are less precise for these ions. It is believed that the structure of the basal siloxane surface is

444   formed of ditrigonal cavities (Tesson *et al.,* 2016), rather than the hexagonal cavities observed in

445   these simulations. This suggests a limitation in the force field used within these calculations. The

446   recently developed polarizable force field (Tesson *et al.,* 2016) is parameterized to accurately

447   reproduce the ditrigonal structure of a clay mineral surface, and may be a more suitable choice

448   going onwards with further binding energy calculations. Also, the Interface force field (Heinz *et*

449   *al.,* 2013) which includes explicit bonding between surface atoms and dissimilar atom types for

450   basal oxygen atoms, may be more suited to this task.

451

452   ***Equilibrium Constants and Determining a Hofmeister Series for the basal surface of***

453   ***Montmorillonite:***

454   To compare binding energies between divalent and monovalent cations at basal surfaces

455   it is required to divide the divalent binding affinity by two (or double the monovalent value)

456   since it takes two monovalent ions to replace a single divalent ion in identical clay systems. This

457   is valid assuming that the chemical environments of the two monovalent ions do not overly

458   interact with one another. Following this procedure, the results present a Hofmeister-like series

459   for ion adsorption to smectite mineral surfaces of the form:

$$K^+ > Na^+ > Ca^{2+} > Cs^+ > Ba^{2+}$$
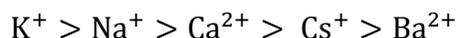
460   Furthermore, the binding energy difference between ion A and B ($\Delta\Delta G_A^B$) can be

461   tabulated by considering the difference in global binding energies between the respective atoms

462   (Table 4). These values are related to the exchange equilibrium constant ($^{ex}K_A^B$) as (Bourg and

463   Sposito, 2011):

464    $\Delta\Delta G = -RT \ln(K)$ (6) where $^{ex}K_A^B$ relates to the equilibrium reaction

465   between clay, cation A and cation B:

466    $A - Clay + B^+ \rightleftharpoons B - Clay + A^+$ (7) The calculated equilibrium constants

467   generally agree with the literature values (Table 5). The $\Delta\Delta G_A^B$ binding energy differences are of

468   the order of the thermal energy at 300K (2.476kJ) or smaller in all instances. Overall, the values

469   of K_A^B and $\Delta\Delta G_A^B$ show that the basal surface of montmorillonite is weakly selective, in

470   agreement with literature results (Bourg and Sposito, 2011).

471

472   **CONCLUSIONS**

473   In this study multiple ensembles of molecular dynamic simulations used in conjunction

474   with well-tempered metadynamics, have been used to form the basis for deriving the adsorption

475   energies and mechanisms of simple ions to hydrated mineral surfaces. The methodology is robust

476   and can be transferred to a wide variety of applications to measure the affinity between mineral

477   surfaces and a marked assortment of organic material. The results immediately suggest further

478   ways to improve the accuracy of the calculation of binding energies to clay mineral surfaces.

479   When calculating the binding energy of poorly hydrating molecules to clay surfaces, such as

480   potassium and cesium, it is critically important to accurately portray the ditrigonal coordination

481   of basal surface oxygens on the siloxane surface.

482   Detailed analysis of the water structure and planar xy density of cations in their

483   energetically favorable states has revealed four separate surface-ion complexations. Both

484   primary and secondary ISSCs are observed for the weakly and strongly hydrated cations

485   respectively. A second hydration shell surface complex, whereby the second hydration shell of

486   the cation overlaps with the first hydration layer of the mineral surface, is observed for sodium.

487   Outer-shell surface complexes are observed to form for the strongly hydrated ions, sodium,

488   barium and calcium.

489   Using the metadynamic algorithm, the results have confirmed the idea of a Hofmeister

490   series for smectite-like minerals. For basal surfaces, the series follows the form:

$$K^+ > Na^+ > Ca^{2+} > Cs^+ > Ba^{2+}$$
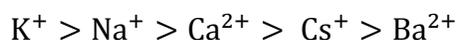
491   and this insight impacts upon a wide range of industrial applications of clay minerals.

492   Finally, the preference for monovalent ions to be adsorbed to the surface over the naturally

493   occurring divalent ions is important for many industrial applications using the cation-exchange

494   mechanism, whereby an inherently present divalent calcium ion is replaced with monovalent

495   cation which can improve, for example, water-wettability, and thus increase oil extraction rates

496   in enhanced oil recovery. Future work entails studying the adsorption of ions as a function of salt

497   concentration, the energetics of intercalated ions as well as the calculating the energy barriers at

498   clay edge sites. Furthermore, the role of tetrahedral substitutions may play a large role in the

499   stability of such ionic systems.

500

BIBLIOGRAPHY

506 Aaqvist, J. (1990). Ion-water interaction potentials derived from free energy perturbation

508 simulations. *The Journal of Phyical Chemistry,* **94**, 8021-8024.

509 Barducci, A., Bussi, B. and Parrinello M. (2008). Well-Tempered Metadynamics: A Smoothly

510 Converging and Tunable Free energy Method. *Physical Review Letters,* **100,** 020603.

511 Benson, L.V. (1982). A tabulation and evaluation of ion exchange data on smectites.

512 *Environmental Geology,* **4**, 23-29.

513 Berendsen, H.J.C, Grigera, J.R. and Straatsma, T.P. (1987). The missing term in effective pair

514 potentials. *The Journal of Physical Chemistry,* **91**, 6269–6271.

515 Bergaya, F., Theng, B. and Lagaly, G. (2006). *Handbook of Clay Science* **(Vol. 1)**. Elsevier

516 Science.

517 Boek, E.S., Coveney, P.V. and Skipper, N.T. (1995). Monte Carlo Molecular Modeling Studies of

518 Hydrated Li-, Na-, and K-Smectites: Understanding the Role of Potassium as a Clay

519 Swelling Inhibitor. *The Journal of the American Chemical Society,* **117**, 12608–12617.

520 Boek, E.S. and Sprik, M. (2003). Ab initio molecular dynamics study of the hydration of a

521 sodium smectite clay. *The Journal of Physical Chemistry B*, **107,** 3251-3256.

522 Bonomi, M., Branduardi, D., Bussi, G., Camilloni, C., Provasi, D., Raiteri, P., Donadio, D.,

523 Marinelli, F., Pietrucci, F., Broglia, R.A. and Parrinello, M. (2009). PLUMED: A portable

524 plugin for free energy calculations with molecular dynamics. *Computer Physics*

525 *Communications*, **180**, 1961-1972.

526 Bowers, G.M., Bish, D.L. and Kirkpatrick, R.J. (2008). H2O and cation structure and dynamics

527 in expandable clays: 2H and 39K NMR investigations of hectorite. *The Journal of*

528 *Physical Chemistry C*, **112,** 6430-6438.

529   Bourg I.C. and Sposito G. (2011). *Ion exchange phenomena*; *Handbook of Soil Science*,

530   *Properties and Processes (2nd Ed.).* CRC Press, Boca Raton.

531   Brown, D.R. and Kevan, L. (1988). Aqueous coordination and location of exchangeable copper

532   (2+) cations in montmorillonite clay studied by electron spin resonance and electron spin

533   echo modulation. *Journal of the American Chemical Society*, **110,** 2743-2748.

534   Chang, F.R.C., Skipper, N.T. and Sposito, G. (1995). Computer simulation of interlayer

535   molecular structure in sodium montmorillonite hydrates. *Langmuir*, **11,** 2734-2741.

536   Chen, C.C. and Hayes, K.F. (1999). X-ray absorption spectroscopy investigation of aqueous Co

537   (II) and Sr (II) sorption at clay–water interfaces. *Geochimica et Cosmochimica Acta*, **63,**

538   3205-3215.

539   Coveney, P.V. and Wan, S. (2016). On the calculation of equilibrium thermodynamic properties

540   from molecular dynamics. *Physical Chemistry Chemical Physics*, **DOI:**

541   10.1039/C6CP02349E.

542   Cygan, R.T., Liang, J.J. and Kalinichev, A.G. (2004). Molecular Models of Hydroxide,

543   Oxyhydroxide, and Clay Phases and the Development of a General Force Field. *The*

544   *Journal of Phyical Chemistry B,* **108**, 1255-1266.

545   Downs, R.T. and Hall-Wallace, M. (2003). The American Mineralogist crystal structure database.

546   *American Mineralogist,* **88**, 247-250.

547   Eisenman, G. (1962). Cation selective glass electrodes and their mode of operation. *Biophysical*

548   *Journal,* **2**, 259-323.

549   Gast, R.G. (1972). Alkali metal cation exchange on Chambers montmorillonite. *Soil Science*

550   *Society of America Journal,* **36**, 14-19.

551   Gast, R.G. (1969). Standard free energies of exchange for alkali metal cations on Wyoming

552   bentonite. *Soil Science Society of America Journal, 33*, 37-41.

553   Greathouse, J.A., Refson, K. and Sposito, G. (2000). Molecular dynamics simulation of water

554   mobility in magnesium-smectite hydrates. *Journal of the American Chemical Society*,

555   **122,** 11459-11464.

556   Greathouse, J.A., Hart, D.B., Bowers, G.M., Kirkpatrick, R.J. and Cygan, R.T. (2015). Molecular

557   Simulation of Structure and Diffusion at Smectite–Water Interfaces: Using Expanded

558   Clay Interlayers as Model Nanopores. *The Journal of Physical Chemistry C,* **119**, 17126–

559   17136.

560   Greenwell, H.C., Jones, W., Coveney, P.V. and Stackhouse, S. (2006). On the application of

561   computer simulation techniques to anionic and cationic clays: A materials chemistry

562   perspective. *Journal of Materials Chemistry ,* **16,** 708-723.

563   Hanshaw, B.B. (1964). Cation-exchange constants for clays from electrochemical measurements.

564   *12th Annual Meeting of the Clay Minerals Society.*

565   Heinz, H., Lin, T.-J., Mishra, R.K. and Emami, F.S. (2013). Thermodynamically Consistent

566   Force Fields for the Assembly of Inorganic, Organic, and Biological Nanostructures: The

567   INTERFACE Force Field. *Langmuir,* **29**, 1754-1765.

568   Hunter, J.D. (2007). Matplotlib: A 2D graphics environment. *Computing in Science and*

569   *Engineering*, **9,** 90-95.

570   Koneshan, S., Lynden-Bell, R.M. and Rasaiah, J.C. (1998). Friction Coefficients of Ions in

571   Aqueous Solution at 25 °C. *The Journal of the American Chemical Society,* **120**, 12041-

572   12050.

573   Marry, V. and Turq, P. (2003). Microscopic simulations of interlayer structure and dynamics in

574   bihydrated heteroionic montmorillonites. *The Journal of Physical Chemistry B*, **107,**

575   1832-1839.

576   Marry, V., Dubois, E., Malikova, N., Breu, J. and Haussler, W. (2013). Anisotropy of water

577   dynamics in clays: insights from molecular simulations for experimental QENS analysis.

578   *The Journal of Physical Chemistry C*, **117,** 15106-15115

579   Michaud-Agrawal, N., Denning, E.J., Woolf, T.B. and Beckstein, O. (2011). MDAnalysis: a

580   toolkit for the analysis of molecular dynamics simulations. *Journal of Computational*

581   *Chemistry*, **32,** 2319-2327.

582   Nakano, M., Kawamura, K. and Ichikawa, Y. (2003). Local structural information of Cs in

583   smectite hydrates by means of an EXAFS study and molecular dynamics simulations.

584   *Applied Clay Science*, **23,** 15-23.

585   Ngouana W., B.F. and Kalinichev, A.G. (2014). Structural Arrangements of Isomorphic

586   Substitutions in Smectites: Molecular Simulation of the Swelling Properties, Interlayer

587   Structure, and Dynamics of Hydrated Cs–Montmorillonite Revisited with New Clay

588   Models. *The Journal of Physical Chemistry C*, **118,** 12758-12773.

589   Papelis, C. and Hayes, K.F. (1996). Distinguishing between interlayer and external sorption sites

590   of clay minerals using X-ray absorption spectroscopy. *Colloids and Surfaces A:*

591   *Physicochemical and Engineering Aspects*, **107**, 89-96.

592   Park, S.H. and Sposito, G. (2002). Structure of water adsorbed on a mica surface. *Physical*

593   *Review Letters*, **89,** 085501.

594   Pronk, S., Páll, S., Schulz, R., Larsson, P., Bjelkmar, P., Apostolov, R., Shirts, M.R., Smith, J.C.,

595   Kasson, P.M., van der Spoel, D. and Hess, B. (2013). GROMACS 4.5: a high-throughput

596   and highly parallel open source molecular simulation toolkit. *Bioinformatics,* **29**, 845-

597   854.

598   Rotenberg, B., Marry, V., Malikova, N. and Turq, P. (2010). Molecular simulation of aqueous

599   solutions at clay surfaces. *Journal of Physics: Condensed Matter,* **22**, 284114.

600   Rotenberg, B., Marry, V., Vuilleumier, R., Malikova, N., Simon, C. and Turq, P. (2007). Water

601   and ions in clays: Unraveling the interlayer/micropore exchange using molecular

602   dynamics. *Geochimica et Cosmochimica Acta,* **71**, 5089-5101.

603   Rotenberg, B., Morel, J.-P., Marry, V., Turq, P. and Morel-Desrosiers, N. (2009). On the driving

604   force of cation exchange in clays: Insights from combined microcalorimetry experiments

605   and molecular simulation. *Geochimica et Cosmochimica Acta,* **73**, 4034-4044.

606   Strawn, D.G. and Sparks, D.L. (1999). The use of XAFS to distinguish between inner-and outer-

607   sphere lead adsorption complexes on montmorillonite. *Journal of Colloid and Interface*

608   *Science*, **216,** 257-269.

609   Shroll, R.M. and Smith, D.E. (1999). Molecular dynamics simulations in the grand canonical

610   ensemble: Application to clay mineral swelling. *The Journal of Chemical Physics*, **111,**

611   9025-9033.

612   Smith, D.E. and Dang, L.X. (1994). Computer simulations of cesium–water clusters: Do ion–

613   water clusters form gas-phase clathrates? *The Journal of Chemical Physics,* **101**, 7873.

614   Smith, D.E. and Dang, L.X. (1994). Computer simulations of NaCl association in polarizable

615   water. *The Journal of Chemical Physics,* **100**, 3757.

616   Suter, J.L., Anderson, R.L., Greenwell, H.C. and Coveney, P.V. (2009). Recent advances in large-

617   scale atomistic and coarse-grained molecular dynamics simulation of clay minerals.

618   *Journal of Materials Chemistry ,* **19,** 2482-2493.

619   Swenson, J., Bergman, R. and Howells, W.S. (2000). Quasielastic neutron scattering of two-

620   dimensional water in a vermiculite clay. *The Journal of Chemical Physics*, **113,** 2873-

621   2879

622   Teppen, B.J. and Miller, D.M. (2006). Hydration Energy Determines Isovalent Cation Exchange

623   Selectivity by Clay Minerals. *Soil Science Society of America Journal,* **70**, 31-40.

624   Tesson, S., Salanne, M., Rotenberg, B., Tazi, S. and Marry, V. (2016). Classical Polarizable Force

625   Field for Clays: Pyrophyllite and Talc. *The Journal of Physical Chemistry C*, **120,** 3749-

626   3758.

627   Tribello, G.A., Bonomi, M., Branduardi, D., Camilloni, C. and Bussi, G. (2014). PLUMED 2:

628   New feathers for an old bird. *Computer Physics Communications,* **185**, 604-613.

629   Underwood, T., Erastova, V., Cubillas, P. and Greenwell, H.C. (2015). Molecular Dynamic

630   Simulations of Montmorillonite–Organic Interactions under Varying Salinity: An Insight

631   into Enhanced Oil Recovery. *The Journal of Physical Chemistry C,* **119**, 7282–7294.

632   Viani, A., Gualtieri, A.F. and Artioli, G. (2002). The nature of disorder in montmorillonite by

633   simulation of X-ray powder patterns. *American Mineralogist ,* **87**, 966-975.

634   William Humphrey, A.D. (1996). VMD: visual molecular dynamics. *Journal of Molecular*

635   *Graphics,* **14**, 33-38.

636   Zhang, P.C., Brady, P.V., Arthur, S.E., Zhou, W.Q., Sawyer, D. and Hesterberg, D.A. (2001).

637   Adsorption of barium (II) on montmorillonite: an EXAFS study. *Colloids and Surfaces A:*

638   *Physicochemical and Engineering Aspects*, **190,** 239-249.

639   Zhang, Y. and Cremer, P.S. (2006). Interactions between macromolecules and ions: the

640   Hofmeister series. *Current Opinion in Chemical Biology,* **10**, 658-663.

641

642 Table 1
643 *Binding energies and stable clay-ion separations of cations to montmorillonite basal surfaces. The global energy minimum for each*
644 *ion is bolded. Clay-ion separation values are given in Angstrom and Binding Energies are in kJ/mol. The Primary ISSC is defined as*
645 *the inner-sphere complex located above the hexagonal siloxane cavity of the clay, whilst the secondary ISSC is the complex above a*
646 *basal surface oxygen.*
647

Ion	VdW Radii	Primary ISSC		Secondary ISSC		OSSC		SHSSC	
		Separation	Energy	Separation	Energy	Separation	Energy	Separation	Energy
Na^+	2.35		-	2.3	-2.76 (0.43)	**3.8**	**-9.00 (0.35)**	6.0	-3.68 (0.37)
K^+	3.33	**1.3**	**-10.56 (1.29)**	2.6	-2.46 (0.70)	4.7	-3.83 (0.37)		-
Cs^+	3.83	**2.0**	**-8.34 (0.40)**	2.7	-7.51 (0.38)	4.6	-4.64 (0.26)		-
Ca^{2+}	2.87		-		-	**3.8**	**-16.76 (0.41)**		-
Ba^{2+}	3.81	1.9	+18.26 (3.55)	*2.6*	*-0.54 (1.82)*	**4.2**	**-16.66 (1.46)**	5.8	-8.38 (1.25)

648
649
650 Table 2
651 *The atomic radii and therefore charge to size ratio for each ion. The hydrated radii are calculated as the first minima in the RDF of*
652 *each respective ion. The stable surface complex of each ion is linked to the size of the ion's hydration radii and thus charge to size*
653 *ratio.*
654

Ion	Atomic Radii	Charge/Size ratio	Hydrated Radii	Stable Complex
Na^+	1.90	0.53	3.23	OSSC
K^+	2.43	0.41	3.83	ISSC
Cs^+	2.98	0.34	3.87	ISSC
Ca^{2+}	1.94	1.03	3.13	OSSC
Ba^{2+}	2.53	0.79	3.49	OSSC

Table 3

The coordination number of each ion in each surface complexation state. Expected coordination numbers are taken from (Varma, 2006).

Species	Expected CN	Observed CN	Clay CN	Water CN	Percentage Clay	Percentage Water
Primary ISSC						
Na^+	5	-	-	-	-	-
K^+	6	9.3	5.9	3.4	64%	36%
Cs^+	7	11.8	5.9	5.9	50%	50%
Ca^{2+}	5-7	-	-	-	-	-
Ba^{2+}	5-7	8.5	1.1	7.4	13%	87%
Secondary ISSC						
Na^+	5	5.9	1.1	4.8	19%	81%
K^+	6	7.6	1.9	5.7	25%	75%
Cs^+	7	9.4	2.7	6.7	29%	71%
Ca^{2+}	5-7	-	-	-	-	-
Ba^{2+}	5-7	8.5	1.1	7.4	13%	87%
OSSC						
Na^+	5	5.9	0	5.9	0%	100%
K^+	6	7.6	0	7.6	0%	100%
Cs^+	7	9.3	0	9.3	0%	100%
Ca^{2+}	5-7	8	0	8	0%	100%
Ba^{2+}	5-7	9	0	9	0%	100%
SHSSC						
Na^+	5	5.8	0	5.8	0%	100%
K^+	6	-	-	-	-	-
Cs^+	7	-	-	-	-	-
Ca^{2+}	5-7	8	0	8	0%	100%
Ba^{2+}	5-7	9	0	9	0%	100%
Bulk						
Na^+	5	5.9	0	5.9	0%	100%
K^+	6	7.8	0	7.8	0%	100%
Cs^+	7	8.2	0	8.2	0%	100%
Ca^{2+}	5-7	8	0	8	0%	100%
Ba^{2+}	5-7	9	0	9	0%	100%

Table 4
The binding energy difference ($\Delta\Delta G_A^B$) between ion species.

$\Delta\Delta G_A^B$	Na^+	K^+	Cs^+	Ca^{2+}	Ba^{2+}
Na^+	**0.00**	-1.56	0.66	0.62	0.67
K^+	1.56	**0.00**	2.22	2.18	2.23
Cs^+	-0.66	-2.22	**0.00**	-0.04	0.01
Ca^{2+}	-0.62	-2.18	0.04	**0.00**	0.05
Ba^{2+}	-0.67	-2.23	-0.01	-0.05	**0.00**

Table 5
The exchange equilibrium constants ($^{ex}K_A^B$) for each ion exchange reaction. Literature values are presented in bold italics (Bourg and Sposito, 2011) (Benson, 1982).

$^{ex}K_A^B$	Na^+	K^+	Cs^+	Ca^{2+}	Ba^{2+}
Na^+	-	1.87	0.77	0.78	0.76
K^+	0.54 *0.58*	-	0.41	0.42	0.41
Cs^+	1.30 *1.23*	2.44	-	1.02	1.00
Ca^{2+}	1.28 *1.21*	2.40 *1.04*	0.98 *0.26*	-	0.98
Ba^{2+}	1.31 *1.44*	2.45	1.00	1.02	-
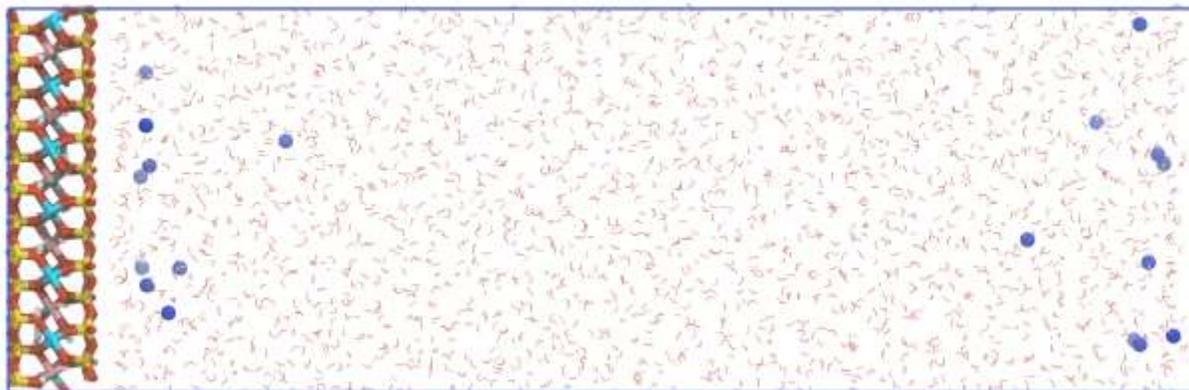
Figure 1: An example supercell used in the simulations. This example is of sodium cations (dark blue) interacting with montmorillonite. The color scheme of the clay is as follows: Silicons are yellow; oxygens are red; aluminums are blue; magnesiums are pink and hydrogens are white. Also presented in stick form are the water molecules within the nano-pore spacing. Periodic boundaries are used in all directions, and the simulation supercell has dimensions approximately 4x4x10 nm (note that the figure is flipped here, such that the z-direction is across the page, from left to right).
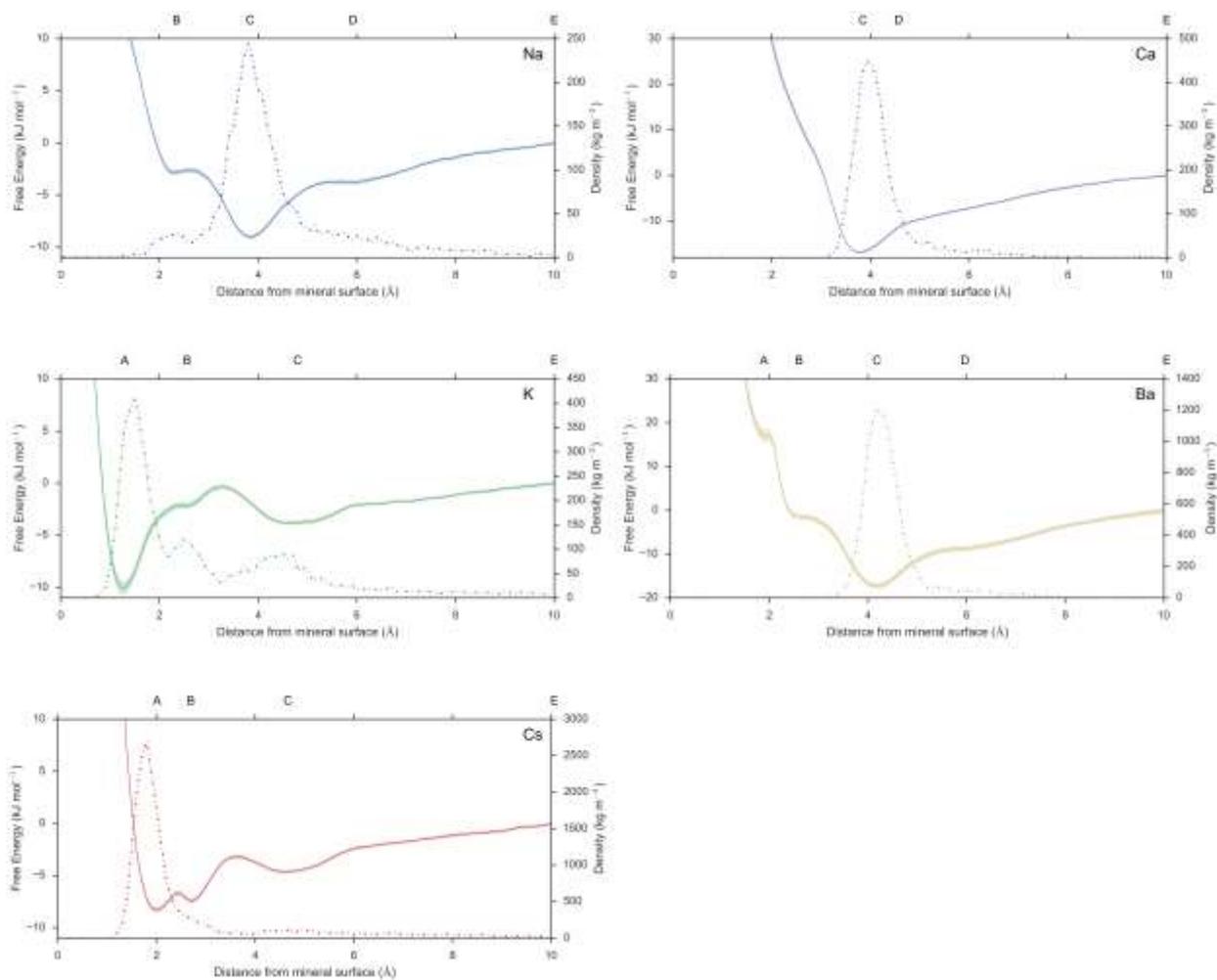
Figure 2: The free energy profile of all cations as a function of clay-ion separation. Note that the shaded region indicates the standard error in the metadynamic calculation at each point along the free-energy diagram. Also presented is the ion density as a function of distance from clay basal surface (dotted line). The points (A), (B), (C) and (D) are noted as interesting features within the free-energy diagram and are shown at the top of the figure.
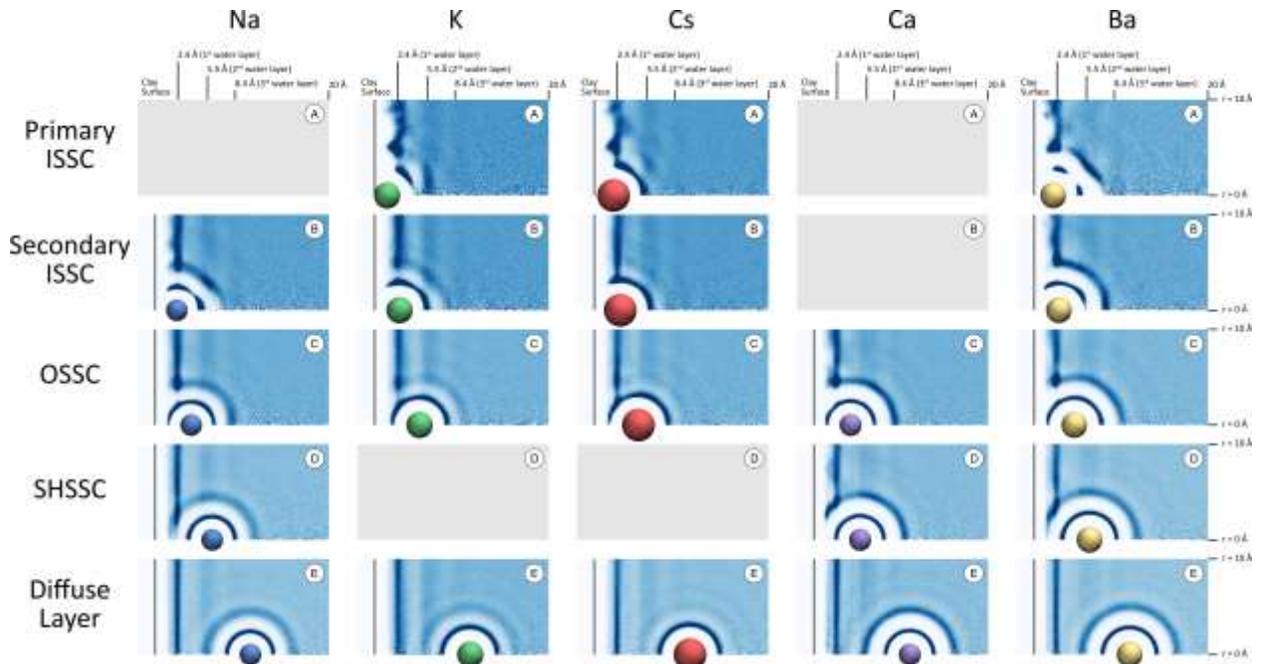
Figure 3: The water oxygen density surrounding the clay and ion at point of interest along the free-energy curve.
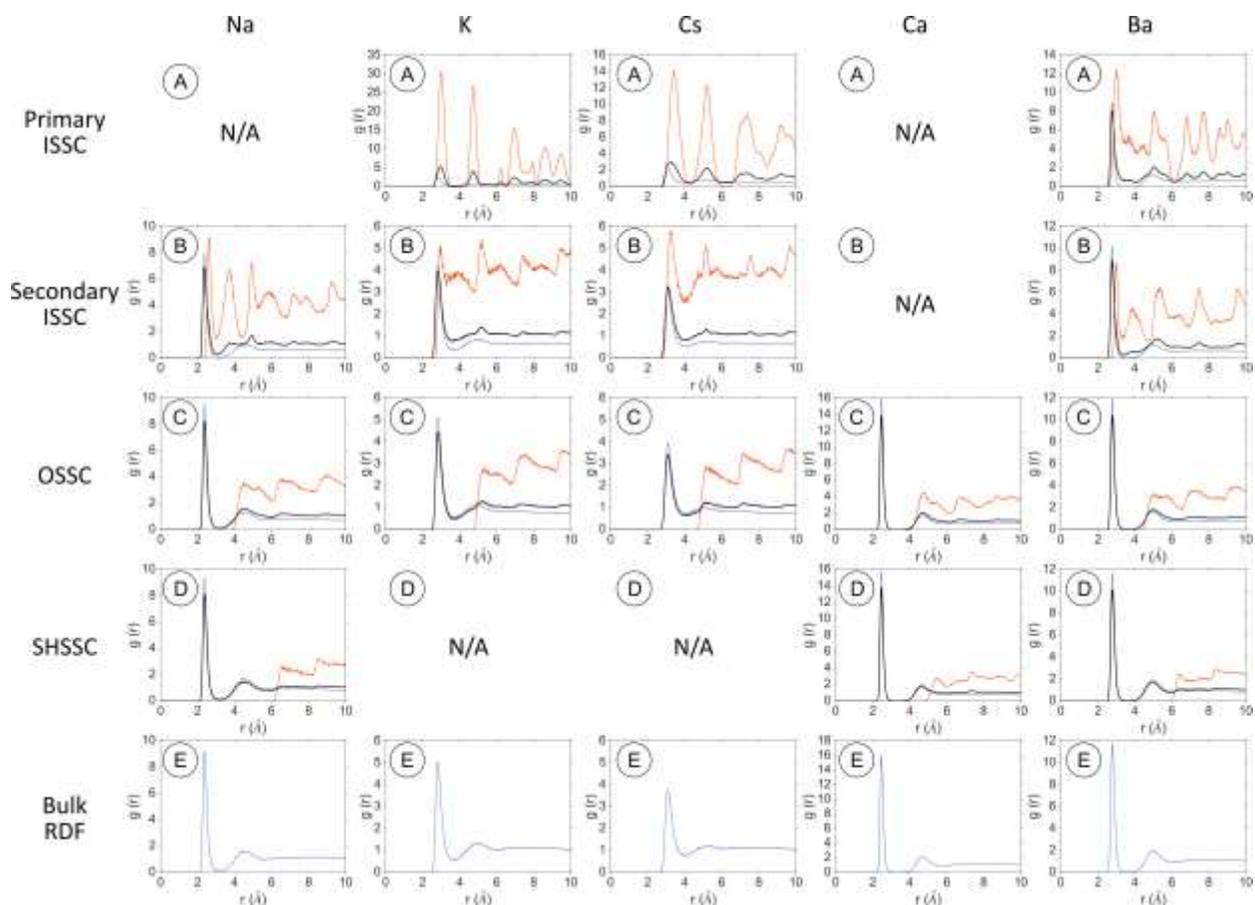
Figure 4: The RDF's between each cation and oxygen atoms at each point of interest along the free-energy diagram. Blue is the RDF between cation and water oxygen, orange is between cation and clay oxygen, and black is the RDF between cation and all oxygen atoms.
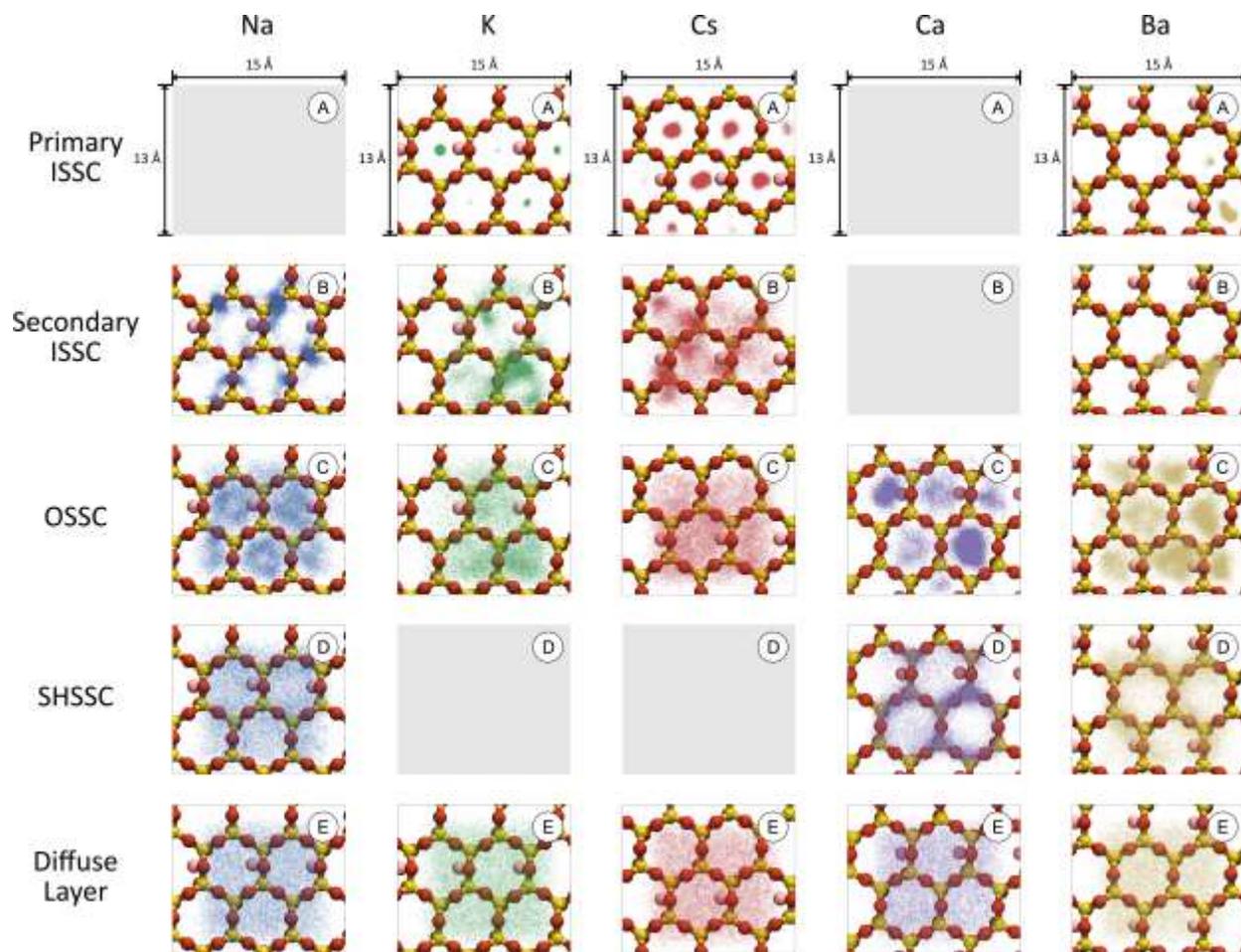
Figure 5:The xy-planar density of the examined cations at each point of interest along the free energy curve.
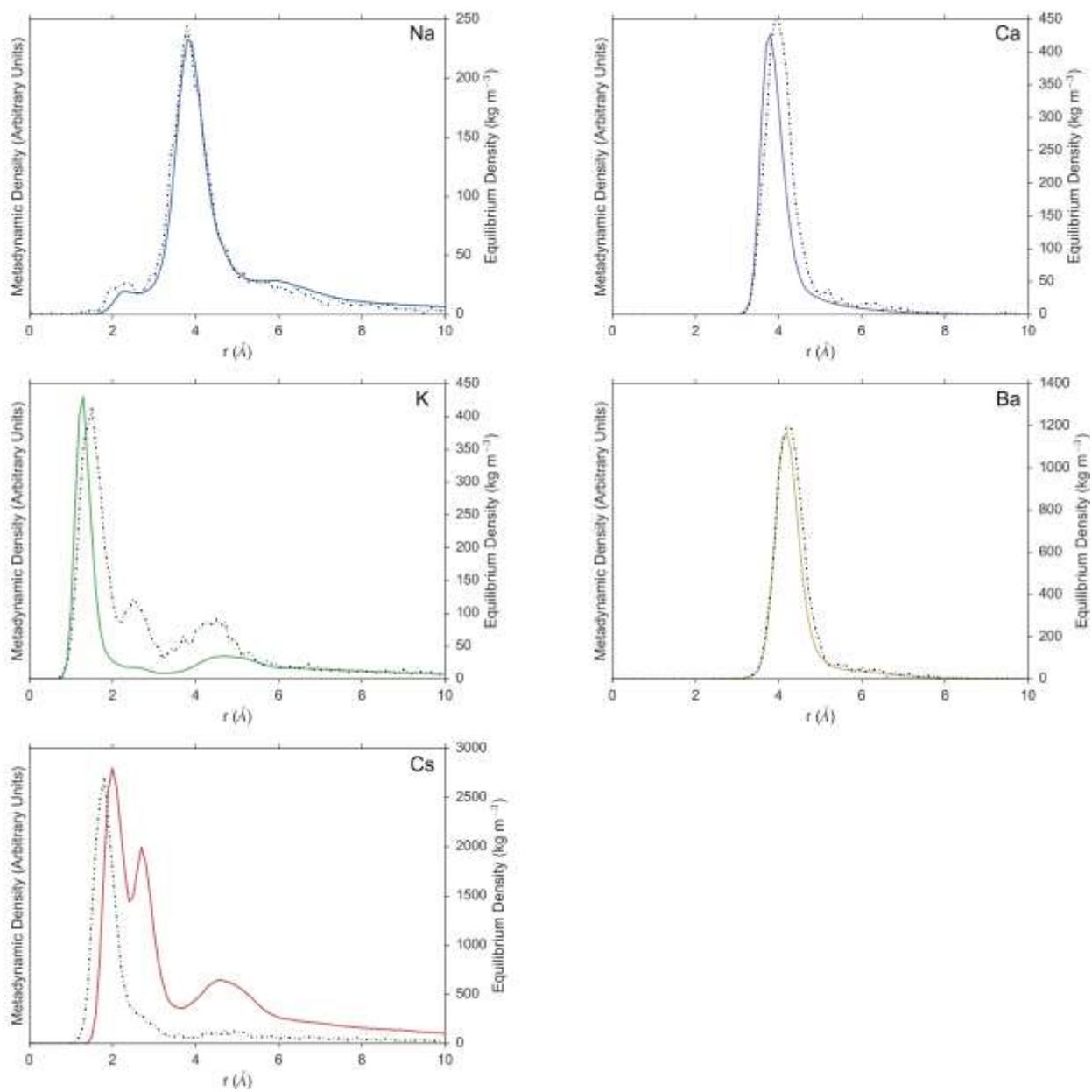
Figure 6: A comparison of ionic densities surrounding the clay surface. Bold colored line is the density calculated from the free energy profile, and the dotted line is the density calculated from an unbiased simulation.